Enhanced Strong Coupling in the Hybrid Dielectric-Metallic Nanoresonator and WS_2 Monolayer

Khalil As'ham,[1] Ibrahim Al-Ani,[1] Mohammed Alaloul,[1] Salah Abdo,[2] Amer Abdulghani,[2] Wen Lei,[3] Haroldo T. Hattori,[1,*] Lujun Huang,[1,†] and Andrey E. Miroshnichenko[1,‡]

[1] *School of Engineering and Information Technology, University of New South Wales at Canberra, Northcott Drive, Canberra ACT 2610, Australia*

[2] *Research Centre of Excellence for Wireless and Photonics Network (WiPNET), Universiti Putra Malaysia, 43400 UPM Serdang, Selangor Darul Ehsan, Serdang, Malaysia*

[3] *School of Electrical, Electronic and Computer Engineering, The University of Western Australia, 35 Stirling Highway Crawley, Western Australia, Crawley WA 6009, Australia*

(Received 4 September 2022; revised 28 March 2023; accepted 14 April 2023; published 15 May 2023)

Exciton polaritons in metallic nanocavities and transition-metal dichalcogenide monolayers has led to striking discoveries, ranging from Bose-Einstein condensation to slowing light. Although plasmonic nanocavities offer small mode volumes, the intrinsic losses of plasmonic nanocavities remain an open challenge in exciton-polariton devices. Consequently, dielectric nanocavities are used as an alternative candidate due to their low intrinsic losses. However, large mode volumes are a central bottleneck in dielectric nanocavities. Here, we theoretically propose to use a hybrid dielectric-metallic nanocavity to enhance light-matter interactions between the excitons of the WS_2 monolayer and the hybrid nanocavity. Such a hybrid nanoresonator inherits the advantages of both dielectric and metallic nanocavities, including ultrasmall mode volume, ultralow losses, and reasonably-high-Q factor. It is demonstrated that the thickness and material of the central gap film together with the thickness of the metallic substrate play vital roles in governing the coupling strength between $1L$-WS_2 excitons and the cavity. After optimizing the geometry and material parameters, the Rabi splitting is increased to 113 meV, almost twice that in dielectric metasystems. The significant improvement can be attributed to the greatly enhanced near field and the ultrasmall mode volume. Furthermore, we show that Rabi splitting can be further boosted to 151 meV by increasing the number of layers of WS_2 and h-BN film in the nanocavity.

DOI: 10.1103/PhysRevApplied.19.054049

I. INTRODUCTION

In recent years, enhancing light-matter interactions between nanophotonic cavities and excitons (exciton polaritons) has drawn much attention due to their widespread applications in strong optical nonlinearity, Bose-Einstein condensation, and low-threshold lasers [1–3]. The light-matter interaction falls within a strong-coupling regime when the decay rates of the optical cavities and excitons are lower than the energy-exchanged rates between these subsystems [4,5]. Usually, the strong coupling is characterized by the Rabi splitting between two polariton branches, which should be larger than the mean linewidth of both systems [6,7].

One of the most widely used nanophotonic cavities for the observation of exciton polaritons is the plasmonic nanocavity due to its ability to confine light in an ultrasmall mode volume [2,8–11]. Although exciton polaritons in metals and various nanosystems, such as J aggregates, molecules, and quantum dots have been reported [12–14], remarkable challenges still remain for this class of nanosystem. For instance, many J aggregates or molecules are needed to observe plexcitons [15], and quantum dots have low stability [1,5,7].

Recently, two-dimensional transition-metal dichalcogenides (TMDCs) have been regarded as an excellent alternative candidate to observe exciton polaritons due to their large binding energy and large quantum yield at room temperature when they are reduced to the monolayer limit [15–20]. Exciton polaritons in the TMDC monolayer and individual metallic nanoparticles have been reported by using either a single or an array of metallic nanostructures [18–22]. These studies open the door to study further strong light-matter interactions between the TMDC monolayer and various single plasmonic nanoparticles, including nanoprisms, nanocubes, and nanodisks [2,5,10,23–27]. However, metal nanocavities themselves suffer from considerable intrinsic loss, leading to tremendous

*H.Hattori@adfa.edu.au
†ljhuang@mail.sitp.ac.cn
‡andrey.miroshnichenko@unsw.edu.au

heat generation and degradation of the performance of the polariton nanodevices [28–31]. Moreover, metallic nanocavities usually support low-order plasmonic resonances, such as the electric dipolar resonance, and thus, have a low quality factor [28].

To address material losses in the metallic cavities, dielectric nanocavities made of high-refractive-index semiconductors have been used as an alternative candidate to observe exciton polaritons [32–40]. On one hand, they have an ultralow material loss. On the other hand, they support multipolar electric and magnetic Mie resonances, bringing much freedom in designing high-performance photonic devices. Accordingly, strong coupling is demonstrated between the excitons of TMDCs and various dielectric nanocavities, such as a single dielectric nanoparticle, and photonic crystal slabs [28,41–52]. Although a large Q factor can be achieved in all-dielectric nanostructures, their large mode volumes prevent researchers from realizing ultrastrong coupling with a large Rabi splitting, which may limit applications.

Yet, hybrid nanostructures offer the advantages of both high-index dielectric nanocavities and plasmonic nanocavities with lower intrinsic losses and small mode volumes. To date, only a few studies have investigated the exciton polaritons in TMDCs and hybrid nanocavities. For example, hybrid exciton-cavity plasmonic resonances are enabled in hybrid structures consisting of multilayer-grating TMDCs placed on gold substrate [53], which simultaneously support the Mie resonance and plasmonic resonance. Besides, a few studies also report the light-matter interaction between the Mie resonance and plasmonic resonances in hybrid dielectric-plasmonic nanocavities [41,54–56]. However, only low-Q Mie resonances are used in these hybrid systems. Thus, combining both the relatively-high-Q Mie resonances with low loss and a small mode volume is desired to enhance the strong coupling between excitons in the TMDC monolayer and photonic nanocavities.

Here, we theoretically investigate the strong coupling between excitons in monolayer WS_2 and photonic nanocavities by leveraging a hybrid dielectric-metallic system that consists of a silicon cylinder with finite thickness sitting on the metallic substrate. Such a hybrid nanoresonator can be strongly coupled with excitons in the WS_2 monolayer with a large Rabi splitting of 79.16 meV, which is much larger than the Rabi splitting in the dielectric-resonator–1L-WS_2 system. The Rabi splitting can be boosted to 125 meV by optimizing the geometry and material parameters, including the thickness and material of the middle dielectric film and metallic thin film supporting the dielectric nanostructures. The significant improvement of the Rabi splitting is ascribed to the increase of the refractive-index contrast and Purcell factor. Moreover, it is found that the Rabi splitting can be further improved to 151 meV by varying the number of layers of WS_2.

II. RESULTS AND DISCUSSION

The open dielectric-dielectric-metal nanocavity used in this work consists of a silicon (Si) nanodisk on a silver (Ag) mirror substrate, between which is the ultrathin SiO_2 film, as shown in Fig. 1(a). The structure is chosen to provide high-refractive-index contrast and large energy confinement in the tiny mode volume of the SiO_2 film. Another advantage of this structure stems from the low losses of the hybrid nanostructure. The parameters of the Si, SiO_2, and Ag materials are extracted from Refs. [57,58].

To understand the nature of the hybrid resonances of this structure, plasmonic dispersion relationships of a multilayer structure of $Si/SiO_2/Ag$ are calculated, as shown in the inset of Fig. 1(b). The permittivity of SiO_2 is 2.1025, whereas Ag permittivity is extracted from the Drude model [57] expressed by $\varepsilon = \varepsilon_\infty - (\omega_p^2/\omega(\omega + i\gamma_p))$, with ε_∞, ω_p, and γ_p being equal to 3.3, 1.35×10^{16} rad/sec, and 3.34×10^{13} rad/sec, respectively. The thickness of Si is identical to the height of the Si nanodisk.

Since the geometry shown in the inset of Fig. 1(b) is infinite in the y direction and the hybrid mode propagates in the x direction, it can be observed that the hybrid resonance has no y-field dependence nor TM polarization due to its plasmonic nature. As a result, the fields E_x, E_z, and H_y all have nonzero values. After calculating hybrid mode solutions by solving Maxwell equations in each layer, the dispersion relationship in Fig. 1(b) can be obtained as [59,60]

$$\left(\frac{k_2}{\varepsilon_2} + \frac{k_3}{\varepsilon_3}\right)\left(\frac{k_2}{\varepsilon_2} + \frac{k_1}{\varepsilon_1}\right) = \left(\frac{k_2}{\varepsilon_2} - \frac{k_3}{\varepsilon_3}\right)\left(\frac{k_2}{\varepsilon_2} - \frac{k_1}{\varepsilon_1}\right) e^{-2k_2 T}. \tag{1}$$

The wave numbers in the three-layered planar nanostructure, k_1, k_2, and k_3, are described by $k_i = \sqrt{k^2 - k_0^2 \varepsilon_i}, i = 1, 2,$ and 3, where T, k, and k_0 are the glass thickness, propagation constant, and wave number in a vacuum, respectively. Here, we fix the height of the Si nanodisk as 70 nm but sweep its radius, and the hybrid modes can be calculated accordingly with Eq. (1). The mode wave number can be defined by $k_{nm} \cong J_{nm}/R$, where J_{nm} [57] is the mth zero of the nth-order Bessel function of the first kind. The analysis shows that mode (1,1), mode (2,1), and mode (3,1) are redshifted as the radius increases [see the dashed lines in Fig. 1(c)]. The results are in good agreement with numerical simulations carried out with the Lumerical FDTD package, as shown in the scattering-efficiency mapping in Fig. 1(c). All the hybrid resonances exhibit a large field enhancement, ranging from 89-fold to 125-fold, at a small mode volume in the SiO_2 film, as presented in the electric field distributions in Figs. 1(d)–1(f). It can be clearly seen that the mode profiles of these hybrid resonances are referred to as mode 11, mode 21, and mode 31.

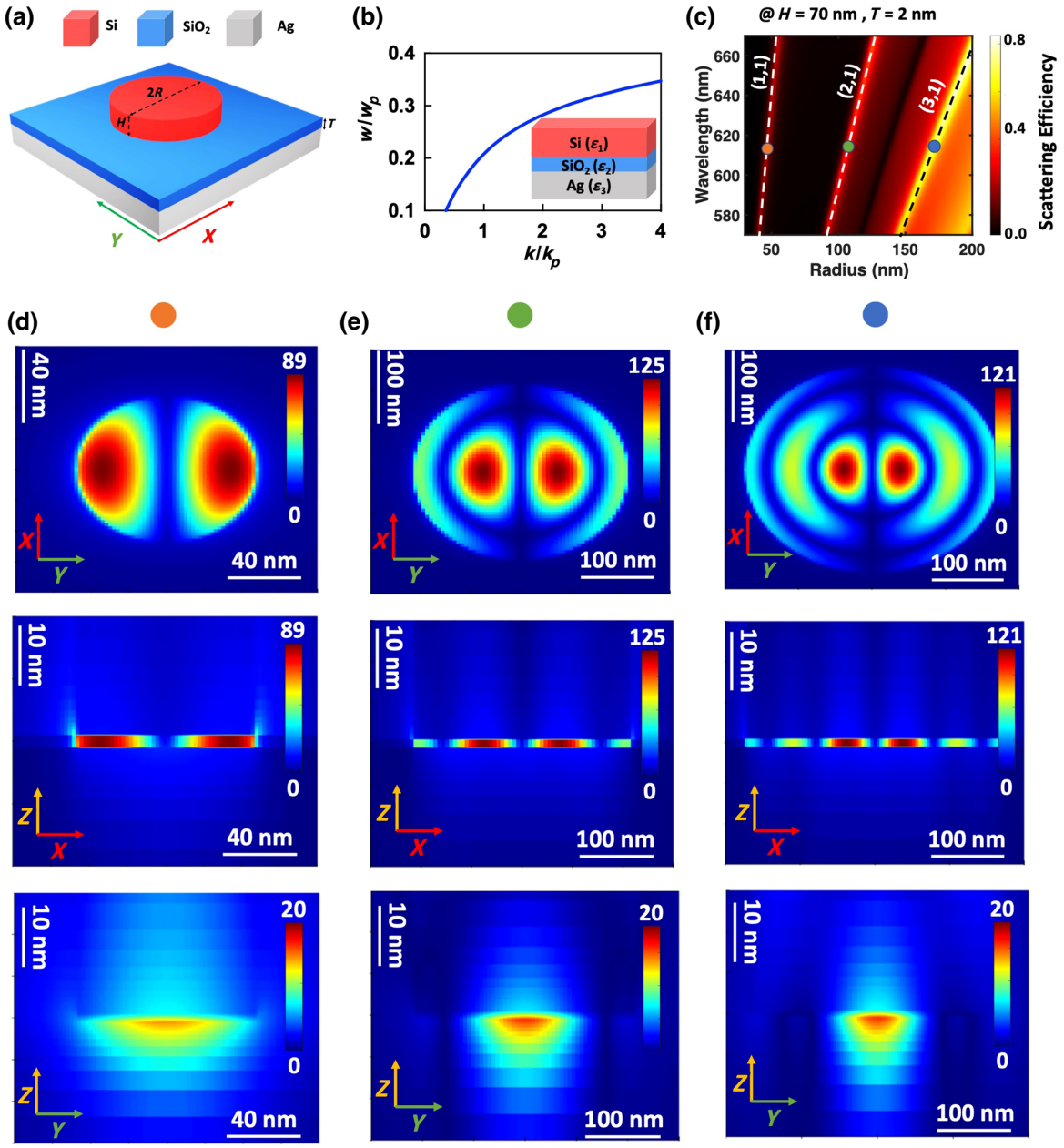

FIG. 1. (a) Schematic drawing of dielectric-metallic nanostructure that consists of Si, SiO_2, and Ag. (b) Dispersion curve of three-layered planar geometry when the Si height is fixed at 70 nm and the SiO_2 thickness is 2 nm. (c) Scattering-efficiency map of Si-SiO_2-Ag nanostructure when the nanodisk radius is tuned from 30 to 200 nm. Dashed lines represent analytical calculations of hybrid modes based on Eq. (1). Electric field distribution of Si-SiO_2-Ag nanostructure at x plane, y plane, and z plane at 616 nm for (d) mode 11, (e) mode 21, and (f) mode 31.

Further calculations are performed to better analyze the three hybrid resonances by calculating the scattering and absorption efficiencies at a wavelength of 616 nm, which corresponds to the exciton resonance wavelength of the WS_2 monolayer. In principle, both scattering and absorption efficiencies are increased as the hybrid-mode order increases from mode 11 to mode 31, as shown in Figs. 2(a)–2(c). Multipole decomposition analysis is performed to reveal the nature of these three hybrid resonances. It can be found from Figs. 2(d)–2(f) that these three resonances are dominated by the magnetic dipole (MD), magnetic dipole-electric dipole, and electric dipole (ED). Additionally, we also calculate their Purcell factors, which are used to evaluate the emission rate enhancement of spontaneous emitters placed inside the resonators. From Figs. 2(g)–2(i), it can be found that modes 11 and 21 have larger Purcell factors than mode 31, suggesting that the first two modes favor enhancing the light-matter

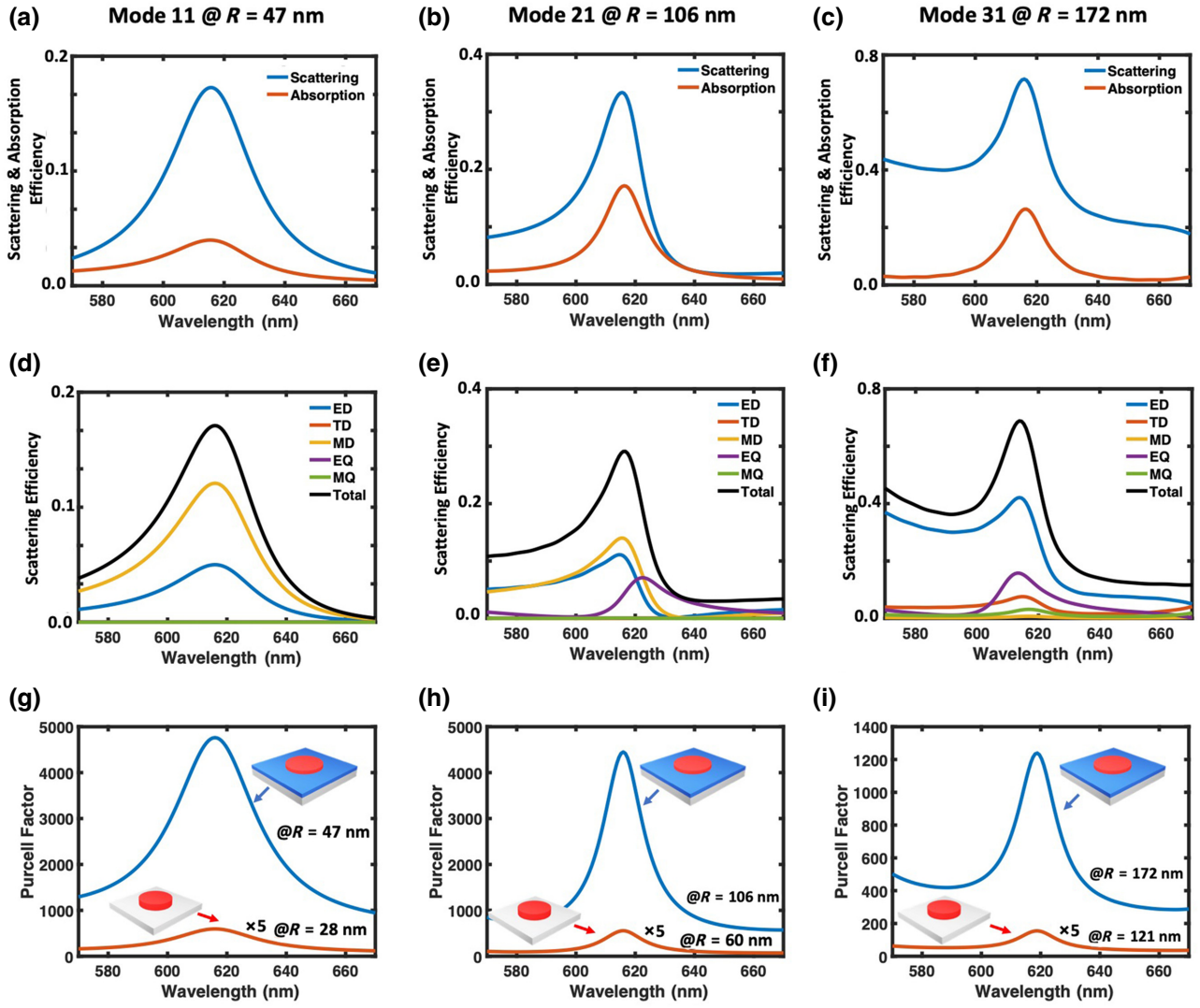

FIG. 2. (a)–(c) Scattering- and absorption-efficiency spectra at 616 nm for mode 11, mode 21, and mode 31, respectively. (d)–(f) Multipole decompaction calculations at 616 nm for mode 11, mode 21, and mode 31, respectively. (g)–(i) Calculated Purcell factors for mode 11, mode 21, and mode 31, respectively. In (g)–(i), red solid lines represent the Purcell factor of Mie resonances. Blue solid lines represent the enhanced Purcell factor of hybrid resonances.

interaction. To show that the hybrid dielectric-metallic resonator indicates better performance in boosting the light-matter interaction, we also calculate the Purcell factor for an isolated Si nanodisk and plot it in Figs. 2(g)–2(i) as a reference. Indeed, all three hybrid resonances have larger Purcell factors than those of pure Mie resonances by 43-, 35-, and 30-fold for mode 11, mode 21, and mode 31, respectively.

Except for the large field enhancement and Purcell factor, the hybrid resonant wavelength can be tuned by varying the radius of the Si nanodisk, as depicted in Figs. 3(b)–3(d). When a two-dimensional (2D) TMDC is placed into the tiny gap between the Si nanoresonator and silver mirror, strong coupling can be induced between their excitons and hybrid resonance. Here, we use the WS_2 monolayer as an example to illustrate this. The permittivity of WS_2 follows the Lorentz oscillator model, as depicted by the real and imaginary parts in Fig. S1 within the Supplemental Material [61,62]. This interesting nanostructure is feasible because it can be fabricated as presented in Fig. S2 within the Supplemental Material [62].

Strong coupling between mode 11 and the exciton in $1L$ WS_2 is evidenced by the anticrossing behavior of two polariton branches, as shown in Fig. 3(f). Resonant tuning via the radius is also plotted as a reference to confirm that the hybrid resonance indeed crosses the exciton resonance. Similarly, both mode 21 and mode 31 exhibit strong-coupling regimes when WS_2 is embedded at the middle-film center, as shown in Figs. 3(g) and 3(h). By comparing the Rabi splitting of the strong coupling

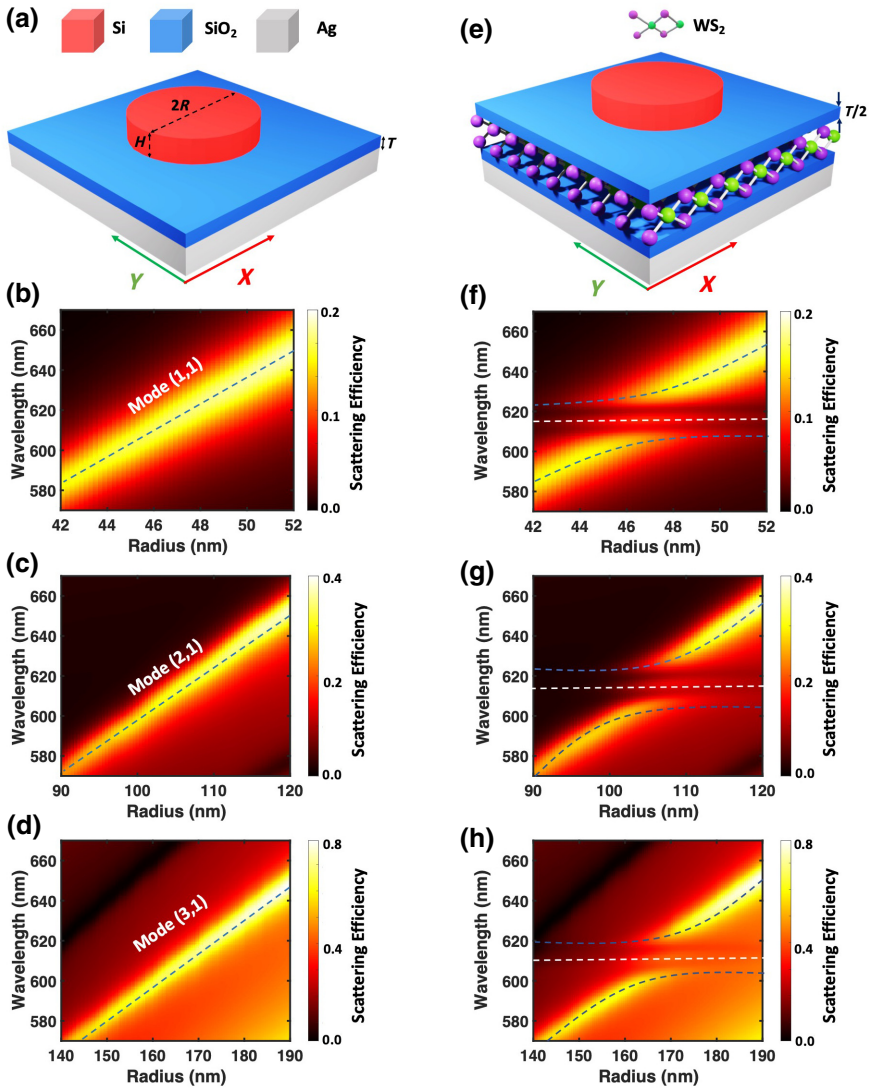

FIG. 3. (a) Schematic of the Si-SiO_2-Ag hybrid structure. (b)–(d) Scattering-efficiency maps of uncoupled mode 11, mode 21, and mode 31, respectively. (e) Schematic of the Si-SiO_2-Ag hybrid structure with WS_2 embedded in the center of the middle-film SiO_2. (f)–(h) Scattering-efficiency maps of strong coupling between hybrid modes (mode 11, mode 21, and mode 31) and excitons.

between three hybrid modes and the exciton, the strong-coupling regime in mode 11 shows the largest Rabi splitting of 79.16 meV among the three exciton polaritons because it has the lowest mode volume of 0.6×10^{-23} m^3 and largest Purcell factor compared with other hybrid modes. The mode volume of this nanostructure is calculated using FDTD via [21,63]

$$v = \frac{\int \varepsilon(R)|E(R)|^2 dv}{\max[\varepsilon(R)|E(R)|^2]}, \tag{2}$$

where $\varepsilon(R)$ and $E(R)$ are the permittivity and the electric field of the multilayer planer nanostructure, respectively.

Here, it is worth pointing out that the Rabi splitting obtained with these three hybrid resonances is much larger than its counterpart in pure dielectric resonators. In contrast to strong coupling between mode 11 and the exciton, the Rabi splitting for mode 31 is 73.7 meV because it has a larger mode volume of 2.27×10^{-23} m^3 and a smaller Purcell factor. The exciton polariton for mode 21 has a Rabi splitting of 74.6 meV with a mode volume of 1.4×10^{-23} m^3 and a moderate Purcell factor.

To verify that the system indeed falls within the strong-coupling regime, the two-oscillator coupled model is applied:,

$$\begin{pmatrix} E_{\mathrm{HM}} - i\hbar\Gamma_{\mathrm{HM}} & g \\ g & E_X - i\hbar\Gamma_X \end{pmatrix} \begin{pmatrix} \alpha \\ \beta \end{pmatrix} = E \begin{pmatrix} \alpha \\ \beta \end{pmatrix}, \tag{3}$$

where E_{HM} and E_X are the hybrid mode and the exciton resonance, respectively. $\hbar\Gamma_{\mathrm{HM}}$ and $\hbar\Gamma_X$ are the half width at half maximum of the hybrid mode and exciton, respectively. α and β are the intermixing coefficients of the generated hybrid states. Fitting the scattering-efficiency mapping in Fig. 3 to the two-oscillator coupled model allows us to extract the eigenenergies of the generated hybrid states and the upper and lower polaritons, with an apparent anticrossing behavior, as shown in Figs. S3(a), S3(c), and S3(e) within the Supplemental Material [62]. Moreover, the Hopefield coefficients in Figs. S3(b), S3(d), and S3(f) within the Supplemental Material [62] show that hybrid modes and excitons contribute to forming the upper and lower polaritons.

The interaction between each hybrid mode and exciton falls within the strong-coupling regime, since they satisfy the required conditions. These conditions are defined as follows:

$$g > \frac{|\hbar\Gamma_A - \hbar\Gamma_X|}{2} \quad \text{and} \quad g > \sqrt{\frac{(\hbar\Gamma_A)^2 + (\hbar\Gamma_X)^2}{2}}. \tag{4}$$

Although systems exhibit the strong-coupling regime, the scattering efficiency is not enough to confirm that the systems fall within the strong-coupling regime. Consequently, the absorption efficiency is also calculated, as shown in Fig. S4 within the Supplemental Material [62].

After establishing that a hybrid dielectric-metal resonator can significantly enhance light-matter interactions, we move to optimize the strong coupling by studying the effects of the geometric parameters and material parameters on the Rabi splitting. We first investigate how the strong coupling is affected by the radius of the Si nanodisk. The radius is varied from 45 to 95 nm.

Notably, modes 21 and 31 provide the largest field enhancements at a nanodisk height of 65 nm compared with mode 11, as shown in Fig. 4(a). However, mode 11 has the largest Rabi splitting of 80.3 meV at 65 nm among the three hybrid modes due to its large Purcell factor, as shown in Figs. 4(b) and 4(c).

The SiO_2 film thickness has a huge effect on the strong coupling. As the SiO_2 thickness decreases, the field enhancement, Purcell factor, and Rabi splitting increase, as shown in Figs. 4(d)–4(f). Interestingly, mode 11 shows a saturated Rabi splitting when the SiO_2 thickness is less than 1.75 nm, as presented in Fig. 4(f). Mode 21 has the largest Rabi splitting (86 meV) with a large Purcell factor (18 000) and field enhancement (152-fold) for 1-nm-thick SiO_2, while mode 31 exhibits the smallest Rabi splitting due to its small Purcell factor. Hence, mode 31 is not considered in this study.

Similarly, the Q factors are calculated for hybrid modes at various thicknesses of Si nanodisk and SiO_2 film, as shown in Fig. S5 within the Supplemental Material [62]. The figure clearly shows that the improvement in Q factors follows the Purcell factor for the uncoupled system and then improves the strong coupling after integrating a 2D monolayer with the hybrid structure. Furthermore, Fig. S5 within the Supplemental Material [62] demonstrates that increasing the SiO_2 film thickness has a significant effect on the Q factor.

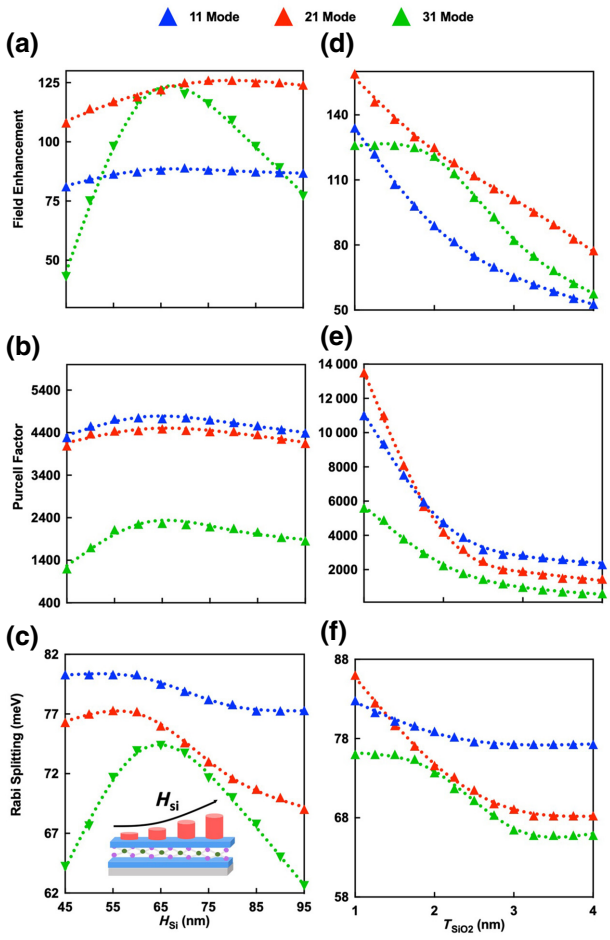

FIG. 4. (a)–(c) Calculated electric field enhancement, Purcell factor, and Rabi splitting when the Si nanodisk height is varied from 45 to 95 nm. (d)–(f) Calculated electric field enhancement, Purcell factor, and Rabi splitting when the middle-film (SiO_2) thickness is varied from 1 to 4 nm. Blue, red, and green tringle dots refer to mode 11, mode 21, and mode 31, respectively.

Since the gap-film thickness has a noticeable effect on the Rabi splitting, it is interesting to study further the effect of various materials on the strong coupling between hybrid modes and excitons. Table I clearly shows that changing the middle-film material can also increase the Rabi splitting of the mode-11–exciton strong coupling from 80.3 to 86.5 meV by using TiO_2. This increase in Rabi splitting is attributed to the increase in the Purcell factor from 4752 to 5487. Similarly, the Rabi splitting for a hybrid system with mode 21 is found to be 93 meV while the Purcell factor is 23 000.

TABLE I. Mode 11 is calculated at 65-nm nanodisk height and 2-nm middle-film thickness, whereas mode 21 is calculated at 70-nm nanodisk height and 1-nm middle-film thickness.

	Material	Field enhancement		Purcell factor		Rabi splitting	
		Mode 11	Mode 21	Mode 11	Mode 21	Mode 11	Mode 21
Middle film	SiO_2	87	152	4752	18 000	80.3	86
	TiO_2	66	76	5487	23 000	86.5	93
	Al_2O_3	78	113	4923	20 000	81	92
	h-BN	76.3	102	5210	21 000	82	92.2
Substrate	Ag	87	152	4752	18 000	80.3	86
	Au	54	33	2291	3000	78	82
	Al	32	24	12 940	1200	76	60

Although changing the substrate material from Ag to Au or Al does not further enhance the strong coupling between hybrid modes and excitons, as shown in Table I, reducing the silver thickness to 100 nm or even lower can further enhance the strong coupling between hybrid modes and excitons. Figure 5(a) shows the effect of reducing the Ag thickness from 100 to 20 nm. As the Ag thickness decreases, the Rabi splitting of the mode-21 exciton increases and reaches its maximum of 99 meV for 20-nm-thick SiO_2 middle film. Since the middle film shows an obvious enhancement in coupling strength, the Rabi splitting is increased to 109 meV and then to 111 meV when Al_2O_3 and *h*-BN are used as middle-film materials, respectively. Interestingly, TiO_2 presents the largest Rabi splitting among all the materials with 125 meV. The increase of Rabi splitting at various Ag thicknesses can be seen in the scattering-efficiency spectra in Fig. 5(d). Electric field enhancement in Fig. 5(b) is calculated with a 1-nm-thick TiO_2 film for 50- and 20-nm-thick Ag films to reveal the physics behind it. It can be clearly seen that the field enhancement in the *z* plane and *y* plane is decreased from 76-fold at 50-nm-thick Ag film to 40-fold at 20-nm-thick Ag film; however, the field enhancement in the *x* plane is increased from 3-fold to 20-fold at 50- and

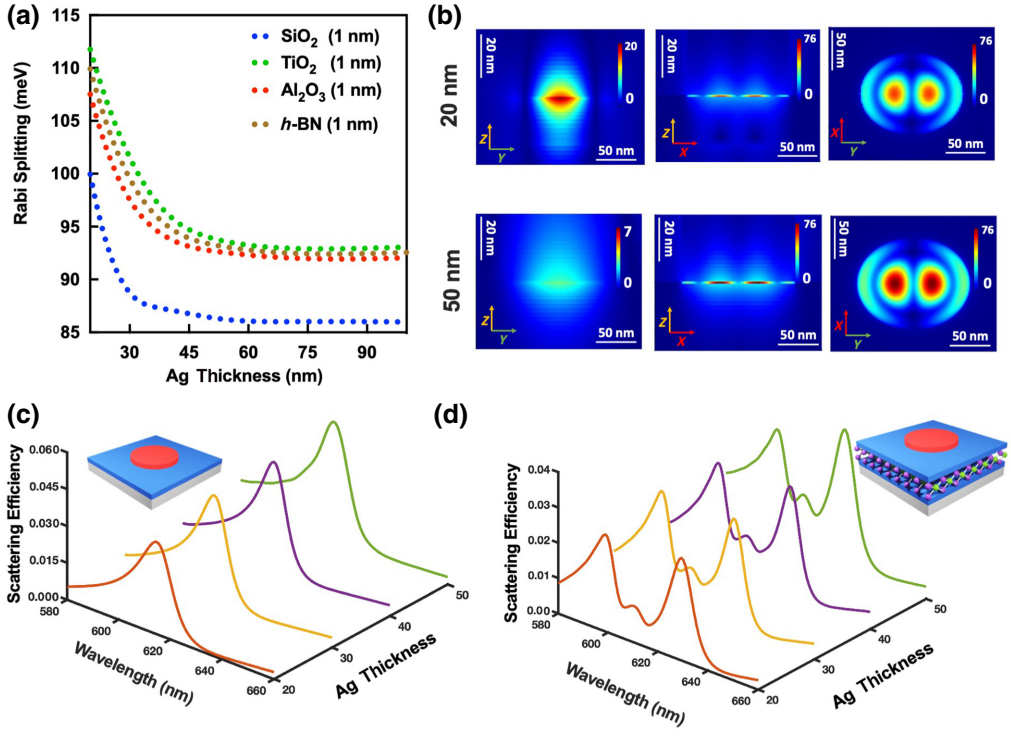

FIG. 5. (a) Rabi splitting as a function of Ag thickness for various middle-film materials, including SiO_2 (blue dots), TiO_2 (green dots), Al_2O_3 (red dots), and TiO_2 (brown dots). (b) Electric field distribution of mode 21 at 20-nm-thick Ag (top panel) and 50-nm-thick Ag (bottom panel). (c) Scattering-efficiency spectra of the uncoupled modes at various Ag thicknesses when the middle-film material is TiO_2. (d) Scattering-efficiency spectra of coupled modes at various Ag thicknesses when WS_2 is put in the center of TiO_2 thin film.

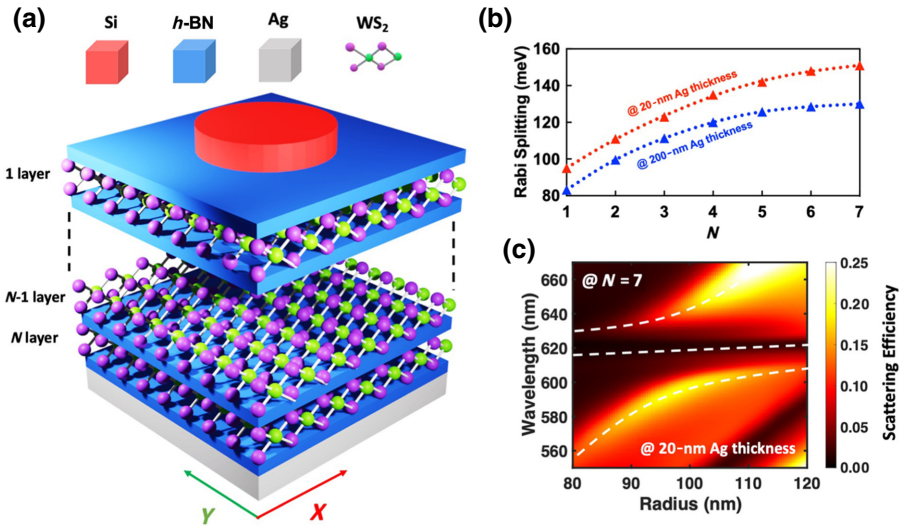

FIG. 6. (a) Schematic of multilayer *h*-BN/WS_2 sandwiched between a Si nanodisk and Ag mirror. Each layer consist of a WS_2 monolayer placed between two 0.65-nm *h*-BN films. (b) Rabi splitting versus number layers of *h*-BN/WS_2 at 200- and 20-nm-thick Ag. (c) Scattering-efficiency mapping of the strong coupling between hybrid resonance (mode 21) and excitons at seven *h*-BN/WS_2 layers and Ag thickness of 20 nm.

20-nm-thick Ag film, respectively. One extra reason for the increase in Rabi splitting is the lower scattering in the far field because the Ag thickness is smaller, as shown in Fig. 5(c).

Last, but not least, hexagonal boron nitride (*h*-BN) is widely used as the substrate for TMDC materials due to its high thermal stability, chemical resistance, and electrical insulation. On the other hand, *h*-BN are also two-dimensional materials, the surfaces of which are free of dangling bonds. The atomic surface smoothness ensures quenched nonradiative recombination due to the lack of surface defects. The integration of *h*-BN and TMDCs can significantly improve the performance of optoelectronic devices based on TMDC monolayers. Several studies demonstrated this improvement by incorporating *h*-BN layers as a substrate or spacer in van der Waals heterostructures of TMDCs [28,64–66]. Thus, it is worthwhile investigating the effect of increasing the number of layers of *h*-BN middle film and WS_2 monolayer from one to seven layers on the strong coupling between mode 21 and the exciton, as shown in the schematic in Fig. 6(a). Each layer of WS_2 has a thickness of 0.7 nm encapsulated between two *h*-BN films of 0.65 nm thick placed on 200-nm Ag. For the case of one layer, the calculated Rabi splitting is 83.4 meV. As the number of layers increases, the Rabi splitting increases and then saturates at six and seven layers with a value of 130 meV, as depicted in Fig. 6(b). At seven layers of WS_2, in which the WS_2 monolayer is sandwiched between two *h*-BN films, the Si nanodisk is tuned from 90 to 130 nm to show the anticrossing behavior of the strong coupling between mode 21 and excitons, as shown in the scattering efficiency in Fig. S6(a) and dispersion relation calculations in Fig. S6(c) within the Supplemental Material [62]. These results are also verified by calculating the absorption efficiency, as shown in Fig. S6(b) within the Supplemental Material [62]. The increase in the Rabi-splitting value is related to the rise in the number of excitons involved in the light-matter interactions between mode 21 and excitons. Similarly, when reducing the Ag thickness from 200 to 20 nm, the Rabi splitting is further boosted to 151 meV, as presented in Fig. 6(b). The scattering-efficiency map is calculated with an obvious anticrossing behavior as shown in Fig. 6(c). The absorption efficiency, dispersion relationship, and Hopefield coefficients prove these results, as depicted in Figs. S7(a)–S7(c) within the Supplemental Material [62].

III. CONCLUSION

We demonstrate an enhanced strong coupling between excitons in the WS_2 monolayer and the hybrid dielectric-metallic nanocavities. By harnessing the advantages of both dielectrics and metals, the Rabi splitting is as high as 79.16 meV. Further optimizing the geometric parameters, such as disk height and gap thickness, and choosing appropriate materials, such as TiO_2 or *h*-BN, significantly improve the Rabi splitting to 93 meV. We also find that the thickness of the thin metallic film underneath plays a vital role in governing the strong coupling. The Rabi splitting can be increased to 113 nm for the 20-nm-thick Ag thin film. Finally, we also find that such a hybrid resonator can significantly boost the light-matter interactions of multilayer WS_2, where a 151-meV Rabi splitting is observed. Given that the hybrid resonances have low loss and a small value, our results may allow us to study nonlinear exciton polaritons.

ACKNOWLEDGMENT

This work is supported by the Australian Research Council (DP200101353).

[1] S. B. Anantharaman, K. Jo, and D. Jariwala, Exciton–photonics: From fundamental science to applications, ACS Nano **15**, 12628 (2021).

[2] M. Geisler, X. Cui, J. Wang, T. Rindzevicius, L. Gammelgaard, B. S. Jessen, P. A. D. Gonçalves, F. Todisco, P. Bøggild, A. Boisen, M. Wubs, N. A. Mortensen, S. Xiao, and N. Stenger, Single-crystalline gold nanodisks on WS_2 mono- and multilayers for strong coupling at room temperature, ACS Photonics **6**, 994 (2019).

[3] J. Cuadra, D. G. Baranov, M. Wersäll, R. Verre, T. J. Antosiewicz, and T. Shegai, Observation of tunable charged exciton polaritons in hybrid monolayer WS_2−plasmonic nanoantenna system, Nano Lett. **18**, 1777 (2018).

[4] S. Wang, S. Li, T. Chervy, A. Shalabney, S. Azzini, E. Orgiu, J. A. Hutchison, C. Genet, P. Samorì, and T. W. Ebbesen, Coherent coupling of WS_2 monolayers with metallic photonic nanostructures at room temperature, Nano Lett. **16**, 4368 (2016).

[5] F. Deng, H. Liu, L. Xu, S. Lan, and A. E. Miroshnichenko, Strong exciton–plasmon coupling in a WS_2 monolayer on Au film hybrid structures mediated by liquid Ga nanoparticles, Laser Photonics Rev. **14**, 1900420 (2020).

[6] J. Sun, Y. Li, H. Hu, W. Chen, D. Zheng, S. Zhang, and H. Xu, Strong plasmon–exciton coupling in transition metal dichalcogenides and plasmonic nanostructures, Nanoscale **13**, 4408 (2021).

[7] M. Stührenberg, B. Munkhbat, D. G. Baranov, J. Cuadra, A. B. Yankovich, T. J. Antosiewicz, E. Olsson, and T. Shegai, Strong light–matter coupling between plasmons in individual gold bi-pyramids and excitons in mono- and multilayer WSe_2, Nano Lett. **18**, 5938 (2018).

[8] H. Pang, H. Huang, L. Zhou, Y. Mao, F. Deng, and S. Lan, Strong dipole-quadrupole-exciton coupling realized in a gold nanorod dimer placed on a two-dimensional material, Nanomaterials **11**, 1619 (2021).

[9] W. Liu, B. Lee, C. H. Naylor, H.-S. Ee, J. Park, A. T. C. Johnson, and R. Agarwal, Strong exciton–plasmon coupling in MoS_2 coupled with plasmonic lattice, Nano Lett. **16**, 1262 (2016).

[10] A. B. Yankovich, B. Munkhbat, D. G. Baranov, J. Cuadra, E. Olsén, H. Lourenço-Martins, L. H. G. Tizei, M. Kociak, E. Olsson, and T. Shegai, Visualizing spatial variations of plasmon–exciton polaritons at the nanoscale using electron microscopy, Nano Lett. **19**, 8171 (2019).

[11] J. J. Baumberg, J. Aizpurua, M. H. Mikkelsen, and D. R. Smith, Extreme nanophotonics from ultrathin metallic gaps, Nat. Mater. **18**, 668 (2019).

[12] P. Vasa, W. Wang, R. Pomraenke, M. Lammers, M. Maiuri, C. Manzoni, G. Cerullo, and C. Lienau, Real-time observation of ultrafast Rabi oscillations between excitons and plasmons in metal nanostructures with J-aggregates, Nat. Photonics **7**, 128 (2013).

[13] R. Chikkaraddy, B. de Nijs, F. Benz, S. J. Barrow, O. A. Scherman, E. Rosta, A. Demetriadou, P. Fox, O. Hess, and J. J. Baumberg, Single-molecule strong coupling at room temperature in plasmonic nanocavities, Nature **535**, 127 (2016).

[14] K. Santhosh, O. Bitton, L. Chuntonov, and G. Haran, Vacuum Rabi splitting in a plasmonic cavity at the single quantum emitter limit, Nat. Commun. **7**, ncomms11823 (2016).

[15] J. Lawless, C. Hrelescu, C. Elliott, L. Peters, N. McEvoy, and A. L. Bradley, Influence of gold nano-bipyramid dimensions on strong coupling with excitons of monolayer MoS_2, ACS Appl. Mater. Interfaces **12**, 46406 (2020).

[16] X. Liu, J. Yi, S. Yang, E.-C. Lin, Y.-J. Zhang, P. Zhang, J.-F. Li, Y. Wang, Y.-H. Lee, Z.-Q. Tian, and X. Zhang, Nonlinear valley phonon scattering under the strong coupling regime, Nat. Mater. **20**, 1210 (2021).

[17] C. Schneider, M. M. Glazov, T. Korn, S. Höfling, and B. Urbaszek, Two-dimensional semiconductors in the regime of strong light-matter coupling, Nat. Commun. **9**, 2695 (2018).

[18] M.-E. Kleemann, R. Chikkaraddy, E. M. Alexeev, D. Kos, C. Carnegie, W. Deacon, A. C. de Pury, C. Große, B. de Nijs, J. Mertens, A. I. Tartakovskii, and J. J. Baumberg, Strong-coupling of WSe_2 in ultra-compact plasmonic nanocavities at room temperature, Nat. Commun. **8**, 1296 (2017).

[19] Y. Sang, C.-Y. Wang, S. S. Raja, C.-W. Cheng, C.-T. Huang, C.-A. Chen, X.-Q. Zhang, H. Ahn, C.-K. Shih, Y.-H. Lee, J. Shi, and S. Gwo, Tuning of two-dimensional plasmon–exciton coupling in full parameter space: A polaritonic non-Hermitian system, Nano Lett. **21**, 2596 (2021).

[20] S. Wang, Q. Le-Van, F. Vaianella, B. Maes, S. Eizagirre Barker, R. H. Godiksen, A. G. Curto, and J. Gomez Rivas, Limits to strong coupling of excitons in multilayer WS_2 with collective plasmonic resonances, ACS Photonics **6**, 286 (2019).

[21] J. Wen, H. Wang, W. Wang, Z. Deng, C. Zhuang, Y. Zhang, F. Liu, J. She, J. Chen, H. Chen, S. Deng, and N. Xu, Room-temperature strong light–matter interaction with active control in single plasmonic nanorod coupled with two-dimensional atomic crystals, Nano Lett. **17**, 4689 (2017).

[22] D. Zheng, S. Zhang, Q. Deng, M. Kang, P. Nordlander, and H. Xu, Manipulating coherent plasmon–exciton interaction in a single silver nanorod on monolayer WSe_2, Nano Lett. **17**, 3809 (2017).

[23] X. Yan and H. Wei, Strong plasmon–exciton coupling between lithographically defined single metal nanoparticles and monolayer WSe_2, Nanoscale **12**, 9708 (2020).

[24] L. Liu, L. Y. M. Tobing, X. Yu, J. Tong, B. Qiang, A. I. Fernández-Domínguez, F. J. Garcia-Vidal, D. H. Zhang, Q. J. Wang, and Y. Luo, Strong plasmon–exciton interactions on nanoantenna array–monolayer WS_2 hybrid system, Adv. Opt. Mater. **8**, 1901002 (2020).

[25] X. Han, K. Wang, X. Xing, M. Wang, and P. Lu, Rabi splitting in a plasmonic nanocavity coupled to a WS_2 monolayer at room temperature, ACS Photonics **5**, 3970 (2018).

[26] B. Munkhbat, D. G. Baranov, A. Bisht, M. A. Hoque, B. Karpiak, S. P. Dash, and T. Shegai, Electrical control

of hybrid monolayer tungsten disulfide–plasmonic nanoantenna light–matter states at cryogenic and room temperatures, ACS Nano **14**, 1196 (2020).

[27] J. Sun, H. Hu, D. Zheng, D. Zhang, Q. Deng, S. Zhang, and H. Xu, Light-emitting plexciton: Exploiting plasmon–exciton interaction in the intermediate coupling regime, ACS Nano **12**, 10393 (2018).

[28] L. Huang, A. Krasnok, A. Alu, Y. Yu, D. Neshev, and A. Miroshnichenko, Enhanced light-matter interaction in two-dimensional transition metal dichalcogenides, Rep. Prog. Phys. **85**, 046401 (2022).

[29] A. Boltasseva and H. A. Atwater, Low-loss plasmonic metamaterials, Science **331**, 290 (2011).

[30] J. B. Khurgin, How to deal with the loss in polasmonics and metamaterials, Nat. Nanotechnol. **10**, 2 (2015).

[31] G. V. Naik, V. M. Shalaev, and A. Boltasseva, Alternative plasmonic materials: Beyond gold and silver, Adv. Mater. **25**, 3264 (2013).

[32] R. Sarma, J. Xu, D. de Ceglia, L. Carletti, S. Campione, J. Klem, M. B. Sinclair, M. A. Belkin, and I. Brener, An all-dielectric polaritonic metasurface with a giant nonlinear optical response, Nano Lett. **22**, 896 (2022).

[33] R. Sarma, N. Nookala, K. J. Reilly, S. Liu, D. de Ceglia, L. Carletti, M. D. Goldflam, S. Campione, K. Sapkota, H. Green, G. T. Wang, J. Klem, M. B. Sinclair, M. A. Belkin, and I. Brener, Strong coupling in all-dielectric intersubband polaritonic metasurfaces, Nano Lett. **21**, 367 (2021).

[34] J. Wang, W. Yang, G. Sun, Y. He, P. Ren, and Z. Yang, Boosting anapole-exciton strong coupling in all-dielectric heterostructures, Photonics Res. **10**, 1744 (2022).

[35] I. A. M. Al-Ani, K. As'ham, O. Klochan, H. T. Hattori, L. Huang, and A. E. Miroshnichenko, Recent advances on strong light-matter coupling in atomically thin TMDC semiconductor materials, J. Opt. **24**, 053001 (2022).

[36] S. You, Y. Zhang, M. Fan, S. Luo, and C. Zhou, Strong light–matter interactions of exciton in bulk WS_2 and a toroidal dipole resonance, Opt. Lett. **48**, 1530 (2023).

[37] P. Xie, Q. Ding, Z. Liang, S. Shen, L. Yue, H. Zhang, and W. Wang, Cavity-assisted boosting of self-hybridization between excitons and photonic bound states in the continuum in multilayers of transition metal dichalcogenides, Phys. Rev. B **107**, 075415 (2023).

[38] M. Qin, J. Duan, S. Xiao, W. Liu, T. Yu, T. Wang, and Q. Liao, Strong coupling between excitons and quasi-bound states in the continuum in bulk transition metal dichalcogenides, Phys. Rev. B **107**, 045417 (2023).

[39] L. Huang, L. Xu, D. A. Powell, W. J. Padilla, and A. E. Miroshnichenko, Resonant leaky modes in all-dielectric metasystems: Fundamentals and applications, Phys. Rep. **1008**, 1 (2023).

[40] L. Huang, L. Xu, M. Rahmani, D. Neshev, and A. E. Miroshnichenko, Pushing the limit of high-Q mode of a single dielectric nanocavity, Adv. Photonics **3**, 016004 (2021).

[41] K. As'ham, I. Al-Ani, L. Huang, A. E. Miroshnichenko, and H. T. Hattori, Boosting strong coupling in a hybrid WSe_2 monolayer–anapole–plasmon system, ACS Photonics **8**, 489 (2021).

[42] Y. Chen, S. Miao, T. Wang, D. Zhong, A. Saxena, C. Chow, J. Whitehead, D. Gerace, X. Xu, S.-F. Shi, and A. Majumdar, Metasurface integrated monolayer exciton polariton, Nano Lett. **20**, 5292 (2020).

[43] R. Verre, D. G. Baranov, B. Munkhbat, J. Cuadra, M. Käll, and T. Shegai, Transition metal dichalcogenide nanodisks as high-index dielectric Mie nanoresonators, Nat. Nanotechnol. **14**, 679 (2019).

[44] S. Lepeshov, M. Wang, A. Krasnok, O. Kotov, T. Zhang, H. Liu, T. Jiang, B. Korgel, M. Terrones, Y. Zheng, and A. Alú, Tunable resonance coupling in single Si nanoparticle–monolayer WS_2 structures, ACS Appl. Mater. Interfaces **10**, 16690 (2018).

[45] H. Wang, J. Wen, W. Wang, N. Xu, P. Liu, J. Yan, H. Chen, and S. Deng, Resonance coupling in heterostructures composed of silicon nanosphere and monolayer WS_2: A magnetic-dipole-mediated energy transfer process, ACS Nano **13**, 1739 (2019).

[46] V. Kravtsov, E. Khestanova, F. A. Benimetskiy, T. Ivanova, A. K. Samusev, I. S. Sinev, D. Pidgayko, A. M. Mozharov, I. S. Mukhin, M. S. Lozhkin, Y. v. Kapitonov, A. S. Brichkin, V. D. Kulakovskii, I. A. Shelykh, A. I. Tartakovskii, P. M. Walker, M. S. Skolnick, D. N. Krizhanovskii, and I. v. Iorsh, Nonlinear polaritons in a monolayer semiconductor coupled to optical bound states in the continuum, Light: Sci. Appl. **9**, 56 (2020).

[47] S. Cao, H. Dong, J. He, E. Forsberg, Y. Jin, and S. He, Normal-incidence-excited strong coupling between excitons and symmetry-protected quasi-bound states in the continuum in silicon nitride–WS_2 heterostructures at room temperature, J. Phys. Chem. Lett. **11**, 4631 (2020).

[48] I. Al-Ani, K. As'Ham, L. Huang, A. Miroshnichenko, and H. Hattori, Enhanced strong coupling of TMDC monolayers by bound state in the continuum, Laser Photonics Rev., 2100240 (2021).

[49] M. Qin, S. Xiao, W. Liu, M. Ouyang, T. Yu, T. Wang, and Q. Liao, Strong coupling between excitons and magnetic dipole quasi-bound states in the continuum in WS_2-TiO_2 hybrid metasurfaces, Opt. Express **29**, 18026 (2021).

[50] L. Huang, B. Jia, Y. K. Chiang, S. Huang, C. Shen, F. Deng, T. Yang, D. A. Powell, Y. Li, and A. E. Miroshnichenko, Topological supercavity resonances in the finite system, Adv. Sci. **9**, 2200257 (2022).

[51] K. Koshelev, G. Favraud, A. Bogdanov, Y. Kivshar, and A. Fratalocchi, Nonradiating photonics with resonant dielectric nanostructures, Nanophotonics **8**, 725 (2019).

[52] M. V. Rybin, K. L. Koshelev, Z. F. Sadrieva, K. B. Samusev, A. A. Bogdanov, M. F. Limonov, and Y. S. Kivshar, High-Q Supercavity Modes in Subwavelength Dielectric Resonators, Phys. Rev. Lett. **119**, 243901 (2017).

[53] H. Zhang, B. Abhiraman, Q. Zhang, J. Miao, K. Jo, S. Roccasecca, M. W. Knight, A. R. Davoyan, and D. Jariwala, Hybrid exciton-plasmon-polaritons in van der Waals semiconductor gratings, Nat. Commun. **11**, 3552 (2020).

[54] K. Du, P. Li, K. Gao, H. Wang, Z. Yang, W. Zhang, F. Xiao, S. J. Chua, and T. Mei, Strong coupling between dark plasmon and anapole modes, J. Phys. Chem. Lett. **10**, 4699 (2019).

[55] F. Deng, H. Huang, J.-D. Chen, S. Liu, H. Pang, X. He, and S. Lan, Greatly enhanced plasmon–exciton coupling in Si/WS_2/Au nanocavities, Nano Lett. **22**, 220 (2022).

[56] S. Shen, Y. Wu, Y. Li, P. Xie, Q. Ding, X. Kuang, W. Wang, and W. Wang, Tuning magnetic Mie-exciton interaction from the intermediate to strong coupling regime in a WSe_2 monolayer coupled with dielectric-metal nanoresonators, Phys. Rev. B **105**, 155403 (2022).

[57] Y. Yang, O. D. Miller, T. Christensen, J. D. Joannopoulos, and M. Soljačić, Low-loss plasmonic dielectric nanoresonators, Nano Lett. **17**, 3238 (2017).

[58] Palik, E. D. *Handbook of Optical Constants of Solids* (Academic press, San Diego, California, 1998), Vol. 3.

[59] S. A. Maier, *Plasmonics: Fundamentals and Applications* (Springer, New York, 2007), Vol. 1.

[60] S. Aldawsari, *Comprehensive theoretical studies of guided modes in multilayer hybrid plasmonic waveguides* (UWSpace, Ontario, Canada, 2018). http://hdl.handle.net/10012/13223.

[61] L. Zhang, R. Gogna, W. Burg, E. Tutuc, and H. Deng, Photonic-crystal exciton-polaritons in monolayer semiconductors, Nat. Commun. **9**, 713 (2018).

[62] See the Supplemental Material at http://link.aps.org/supplemental/10.1103/PhysRevApplied.19.054049 for the real and imaginary parts of the Lorentz oscillator model of WS_2; the steps to prepare the Si-SiO_2-WS_2-Ag hybrid structure; dispersion curves and Hopefield coefficients of strong coupling between excitons and hybrid resonances; absorption-efficiency maps of strong coupling between excitons and hybrid resonances; calculated Q factor for the hybrid mode at different thicknesses of Si nanodisks and SiO_2 films; scattering- and absorption-efficiency maps, dispersion curves, and Hopefield coefficients of strong coupling between excitons and mode 21 at seven layers of WS_2/*h*-BN placed on 200-nm-thick Ag; and absorption-efficiency map, dispersion curve, and Hopefield coefficients of strong coupling between excitons and mode 21 at seven layers of WS_2/*h*-BN placed on 20-nm-thick Ag.

[63] P. Xie, Z. Liang, Z. Li, W. Wang, W. Wang, T. Xu, X. Kuang, L. Qing, D. Li, and J. Yi, Coherent and incoherent coupling dynamics in a two-dimensional atomic crystal embedded in a plasmon-induced magnetic resonator, Phys. Rev. B **101**, 45403 (2020).

[64] F. Cadiz, E. Courtade, C. Robert, G. Wang, Y. Shen, H. Cai, T. Taniguchi, K. Watanabe, H. Carrere, D. Lagarde, M. Manca, T. Amand, P. Renucci, S. Tongay, X. Marie, and B. Urbaszek, Excitonic Linewidth Approaching the Homogeneous Limit in MoS_2-Based van der Waals Heterostructures, Phys. Rev. X **7**, 021026 (2017)..

[65] O. A. Ajayi, J. v Ardelean, G. D. Shepard, J. Wang, A. Antony, T. Taniguchi, K. Watanabe, T. F. Heinz, S. Strauf, X.-Y. Zhu, and J. C. Hone, Approaching the intrinsic photoluminescence linewidth in transition metal dichalcogenide monolayers, 2D Mater. **4**, 031011 (2017).

[66] E. Courtade, B. Han, S. Nakhaie, C. Robert, X. Marie, P. Renucci, T. Taniguchi, K. Watanabe, L. Geelhaar, J. M. J. Lopes, and B. Urbaszek, Spectrally narrow exciton luminescence from monolayer MoS_2 and $MoSe_2$ exfoliated onto epitaxially grown hexagonal BN, Appl. Phys. Lett. **113**, 032106 (2018).